

Characterization of aluminum, aluminum oxide and titanium dioxide nanomaterials using a combination of methods for particle surface and size analysis

B. Krause^{*a}, T. Meyer^b, H. Sieg^c, C. Kästner^d, P. Reichardt^a, J. Tentschert^a, H. Jungnickel^a, I. Estrela-Lopis^b, A. Burel^e, S. Chevance^f, F. Gauffre^f, P. Jalili^g, J. Meijer^h, L. Boehmert^c, A. Braeuning^c, A. F. Thünemann^d, F. Emmerlingⁱ, V. Fessard^g, P. Laux^a, A. Lampen^c and A. Luch^a

^a German Federal Institute for Risk Assessment (BfR), Department of Chemical and Product Safety, Max-Dohrn-Straße 8-10, 10589 Berlin, Germany

^b Institute of Medical Physics and Biophysics, University of Leipzig, Härtelstrasse 16-18, 04275 Leipzig, Germany

^c German Federal Institute for Risk Assessment (BfR), Department of Food Safety, Max-Dohrn-Straße 8-10, 10589 Berlin, Germany

^d Federal Institute for Materials Research and Testing (BAM), Unter den Eichen 87, 12205 Berlin, Germany

^e MRIC TEM BIOSIT, Université de Rennes 1, 2 av pro Leon Bernard, France

^f Institut des Sciences Chimiques de Rennes, UMR-CNRS 6226, Université de Rennes 1, France

^g ANSES, French Agency for Food, Environmental and Occupational Health Safety, Fougères Laboratory, 10B rue Claude Bourgelat, 35306, Fougères Cedex, France

Supporting Information

Figure S1: NTA averaged distributions

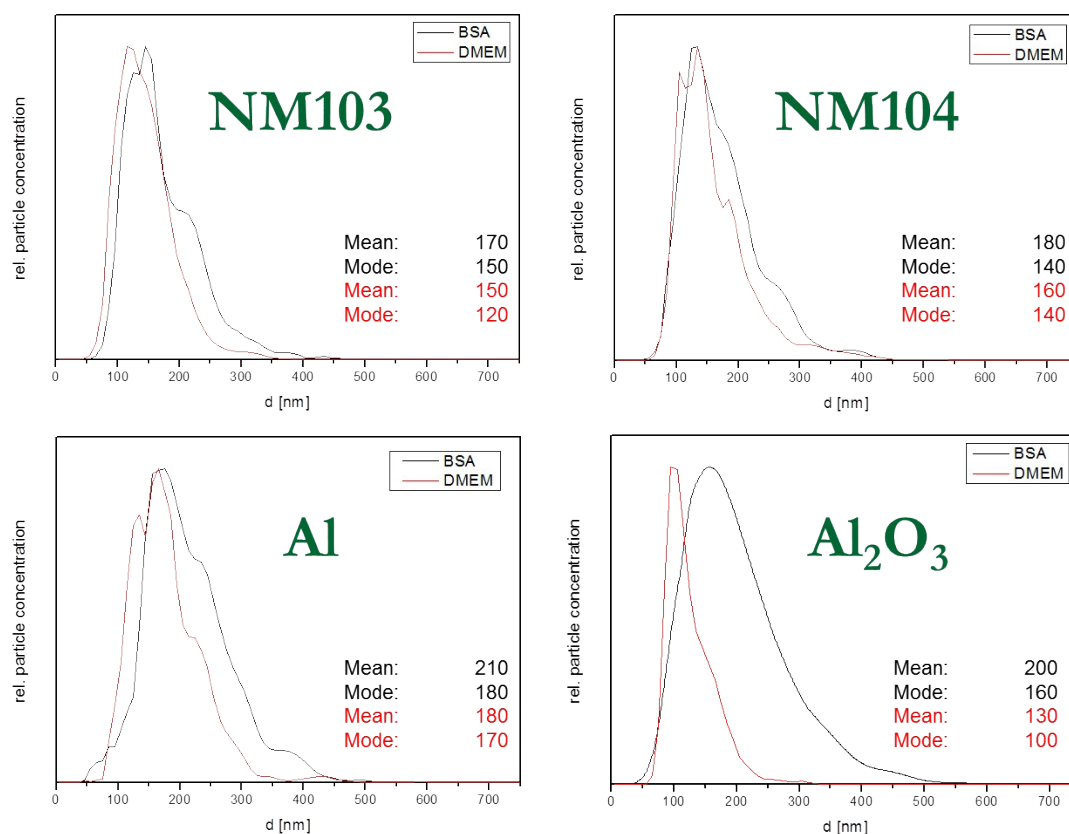


Figure S1: Averaged size distributions of NM103, NM104, Al and Al₂O₃ recorded by NTA. Y-axis: Relative particle concentration; x-axis: hydrodynamic diameter. Black: NMs prepared after Nanogenotox protocol; red: size distribution of NMs under cell culture conditions. BSA: bovine serum albumin; DMEM: Dulbecco's modified eagle medium.

Table S1: Number size distributions by calculation from DLS data

Table S1 Number size distribution with standard deviation (SD) of Al⁰, Al₂O₃, NM103 and NM104 NMs in different media calculated based on the intensity size distribution data determined by dynamic light scattering (DLS). All results represent the average of six repeats. BSA: bovine serum albumin; DMEM: Dulbecco's modified eagle medium; FCS: fetal calf serum

	DLS measurements and comparison	
	Lab 1 (Malvern) Number-based size [nm]	Lab 2 (Brookhaven) Number-based size [nm]
	Stock solution (0.05 % BSA in H ₂ O)	
Al ⁰ NM	240 ± 10	120 ± 30
Al ₂ O ₃ NM	110 ± 10	80 ± 40
NM103	140 ± 10	250 ± 90
NM104	100 ± 10	200 ± 50
	DMEM (with 10 % FCS)	
Al ⁰ NM	160 ± 10	80 ± 10
Al ₂ O ₃ NM	10 ± 1	110 ± 70
NM103	110 ± 10	90 ± 10
NM104	110 ± 10	110 ± 10

The size and size distribution of NMs in number-based DLS measurement mode is interesting for a better comparison with other number-based techniques. To compare DLS data to number-based NTA data, a calculation based on the refractive index and the absorption of the used NMs is possible. While both size distributions are correct, some assumptions need to be taken into account:

- The involvement of the Mie scattering for the more complicated scattering process for particles much smaller than the wavelength of illuminating light (633 nm for Zetasizer ZS, 640 nm for ZetaPALS)
- Known optical properties of the investigated NMs
- good raw data quality (broader distributions or high polydispersity can significantly influence the transition from intensity-based to number based distributions)

In our case, we decided to use the intensity-based distribution only, as there are no assumptions needed compared to the transformation into number-based distributions.

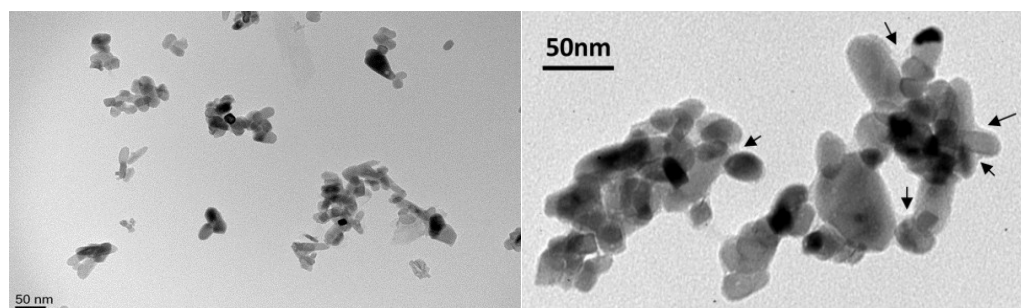
Figure S2: TEM measurement of TiO₂ NMs in DMEM

Figure S2: TEM observation of TiO₂ NMs in BSA (left) and DMEM (right) achieved at 80 kV (0.8 g L⁻¹). Arrows show protein deposition.

Figure S3 – S5: SAXS curves fitted with Monte Carlo based data evaluation

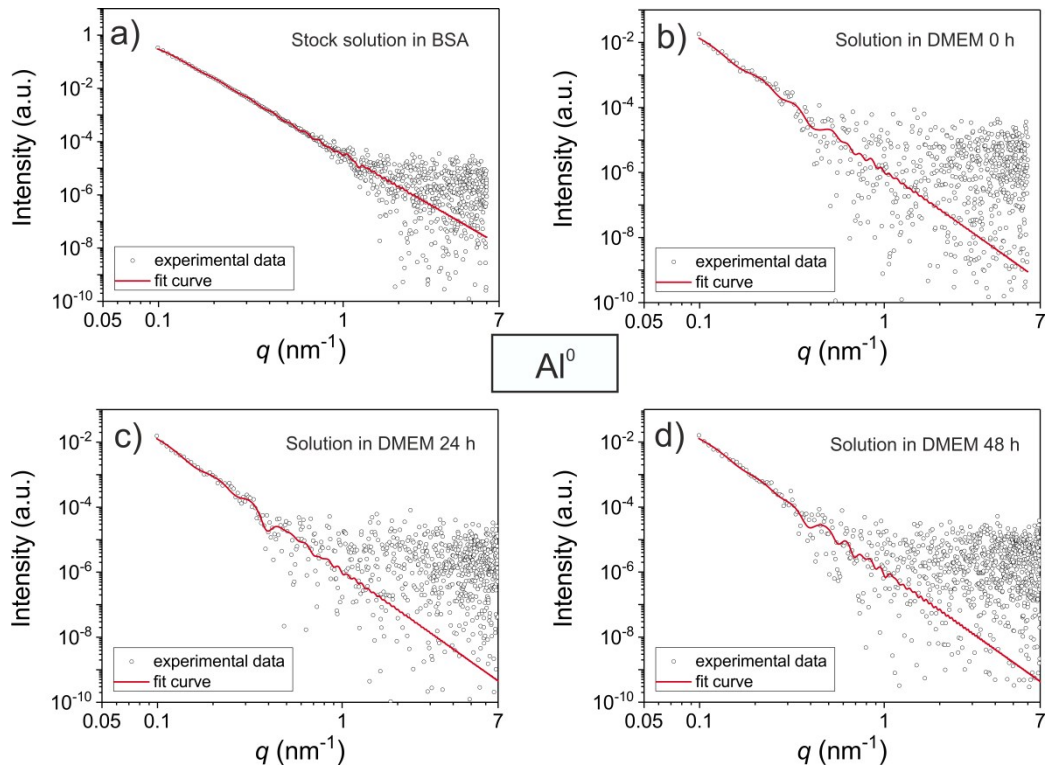


Figure S3: Measured SAXS curves (black circles) of AlI NM in (a) stock solution (BSA), (b) directly after addition in DMEM, (c) after 24 h in DMEM and (d) after 48 h in DMEM. The measured data are fitted with a Monte Carlo based data evaluation (red solid lines).

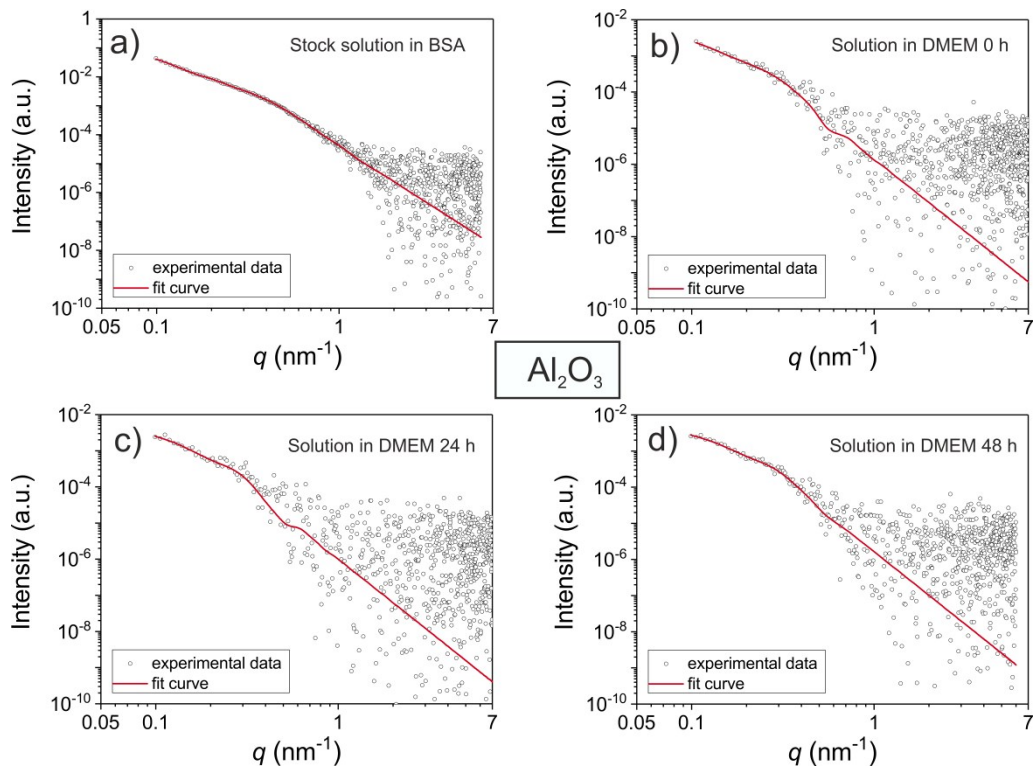


Figure S4: Measured SAXS curves (black circles) of Al_2O_3 NM in (a) stock solution (BSA), (b) directly after addition in DMEM, (c) after 24 h in DMEM and (d) after 48 h in DMEM. The measured data are fitted with a Monte Carlo based data evaluation (red solid lines).

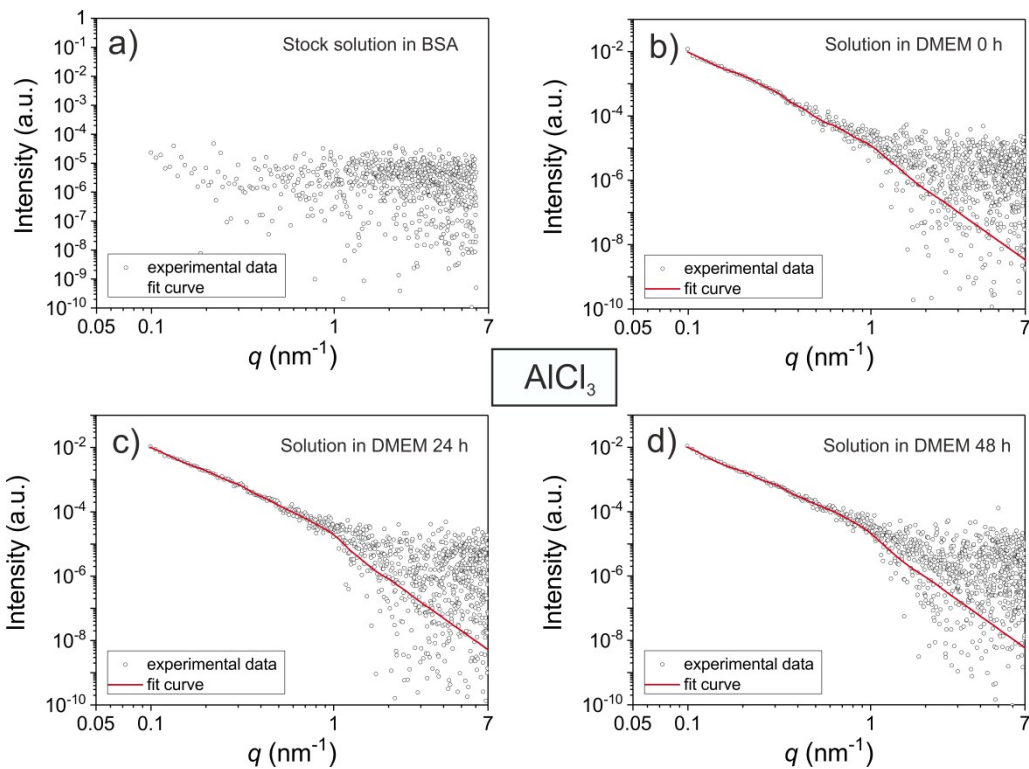


Figure S5: Measured SAXS curves (black circles) of AlCl_3 in (a) aqueous stock solution (b) directly after addition in DMEM, (c) after 24 h in DMEM and (d) after 48 h in DMEM. The measured data are fitted with a Monte Carlo based data evaluation (red solid lines).

Figure S6: Impurities of used NMs determined by IBM

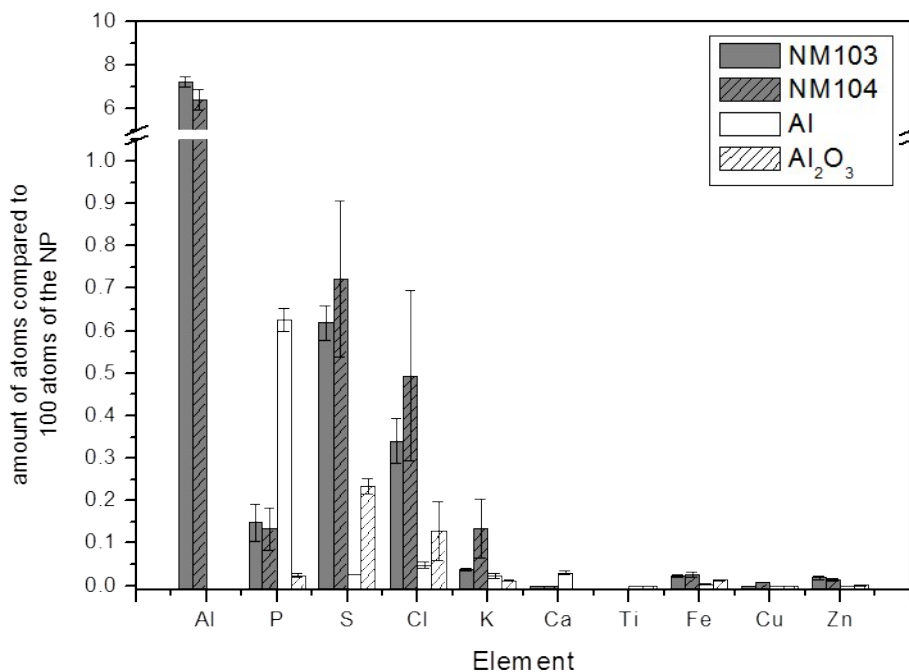


Figure S6: Impurities associated to the NMs as purchased. The impurities are given in number of atoms compared to one hundred atoms of the NMs. In case of TiO_2 titanium isn't shown as well as in case of aluminum containing materials aluminum isn't displayed in the graph.

Figure S7: Aluminum aqua complexes at different pH values

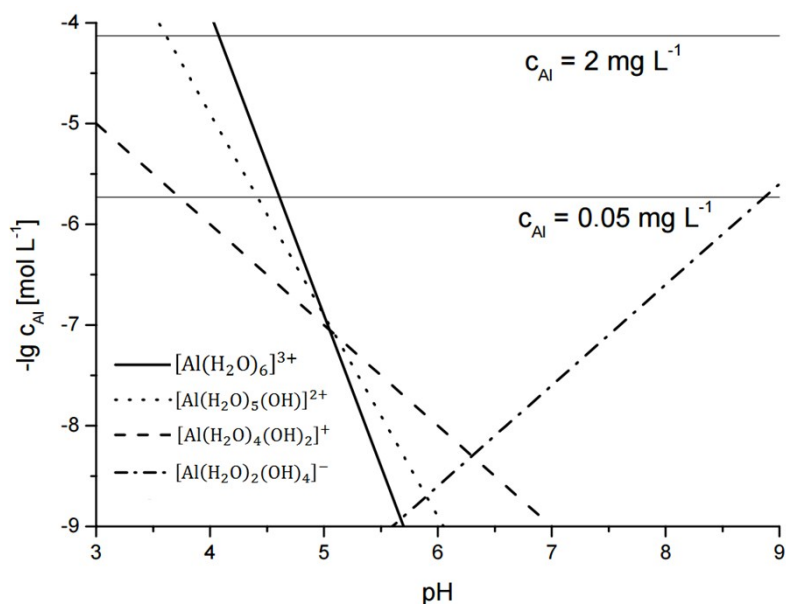


Figure S7: Solubility of Al^{3+} function of pH in equilibrium with $\text{Al}(\text{OH})_{3(s)}$, solubility product of $\text{Al}(\text{OH})_3$ $K_S=10^{-33.9}$ (modified according to Sigg & Stumm 1989) [1].

Figure S8: CRM surface investigations

CRM was applied to study the organic constituents on the surface of the NMs. Figure S8 shows the average Raman spectra of TiO_2 NMs extracted from their spectral images based on the intensity distribution of E_g band of rutile phase, 450 cm^{-1} [2]. The spectra were weighted to integral intensity of NM phonon bands.

For both particles, four main peaks are observable. The peak around 1000 cm^{-1} is a double peak consisting of 988 cm^{-1} induced by ring stretching and 1006 cm^{-1} attributed to ring deformation. These peaks indicate the presence of an aromatic ring structure associated with the particle surface. The region from 1500 to 1700 represents an overlap of different possible structures, e.g. cyclic compounds, double bonds and amide bands [3]. The high variety of possible structures makes clear assignments complicated [3]. The CH_2/CH_3 vibration modes were detected in the region from 2850 to 3000 cm^{-1} attributed to symmetrical and asymmetric CH_2 and CH_3 stretching vibrations and at 1450 cm^{-1} related to $\delta(\text{CH}_2)$ and asymmetric $\delta(\text{CH}_3)$ deformations [3]. These bands can be associated with aliphatic compounds. The Raman spectra of the hydrophobic NM103 revealed a higher concentration of organic surfactants and aromatic compounds on their surface compared to NM104 NMs.

Both NMs exhibit decreased signals of aromatic and aliphatic compounds on their surface after the treatment with ultra-sonic compared to particles without ultra-sonication. This reveals a loss of organic compounds during the ultra-sonication step.

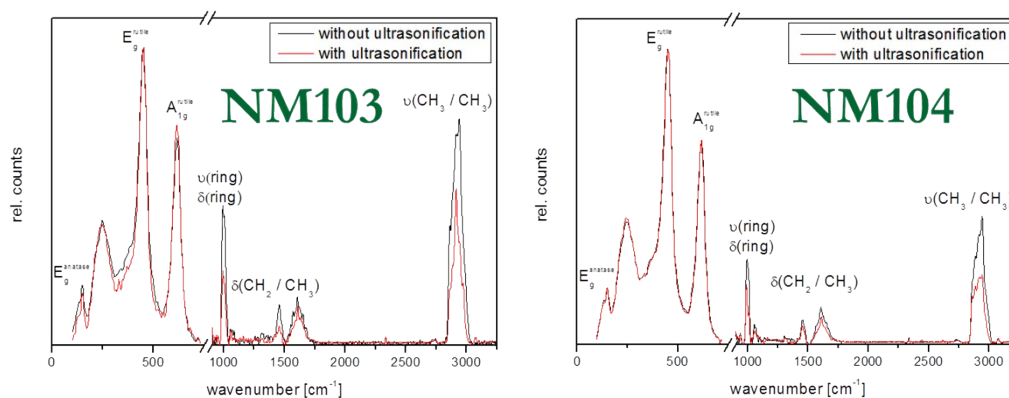


Figure S8: Raman spectra of NMs without and with ultra-sonic treatment. For better visualization, the regions between 900 and 3250 cm^{-1} in both graphs were multiplied by a scaling factor of ten.

Figure S9: Colocalization pattern by IBM

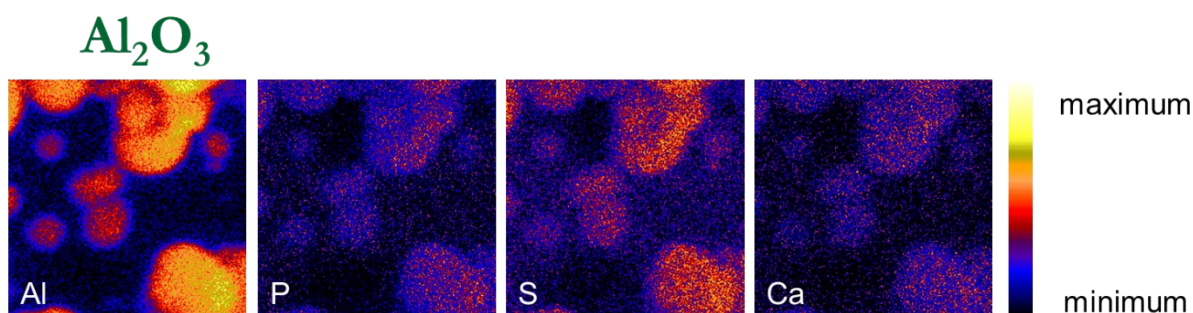


Figure S9: IBM element maps of Al_2O_3 and as purchased only diluted in mpH_2O . The images exhibiting colocalization pattern of the different elements. An area of $50 \times 50 \mu\text{m}^2$ is displayed. The color code is as follows: white represents highest concentration and black the lowest concentration.

Figure S10: Influence of different proteins detected by CRM

The bands associated with CH_2/CH_3 vibration modes exhibit the same extent of intensity decrease for both TiO_2 NMs comparing BSA and DMEM conditions as observed by element analysis (Figure S10). Furthermore, the analysis of phonon bands revealed that the crystal structure of both TiO_2 NMs was not affected during the particle preparation process.

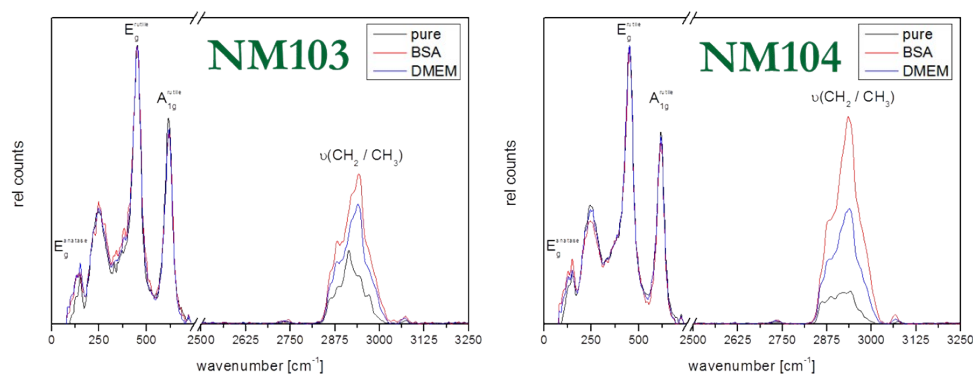


Figure S10: CRM spectra represent the modifications during the preparation process for NM103 (left) and NM104 (right). Pure: particles as purchased; BSA: albumin-coated particles (NanoGenoTOX protocol); DMEM: albumin-coated particles dispersed in DMEM. For better visualization, the regions between 2500 and 3250 cm^{-1} in both graphs were multiplied by a scaling factor of five.

Figure S11 – 14: ToF-SIMS measurements of Al and Al_2O_3 NMs in DMEM

In stock dispersion the albumin concentration is 0.5mg/ml. In DMEM containing FBS the albumin content is about 2mg/ml and about 2.7-4mg/ml other not more specified proteins are included. In addition, the dilution into DMEM was done out of stock dispersion, which already contains 0.5 mg/ml albumin. Using a dilution factor of about 25, 0.02 mg/ml from the BSA stock dispersion, as well as 2 mg/ml albumin and 2.7-4 mg/ml other proteins results in an about 10-times higher protein concentration of DMEM compared to BSA.

Figure S11 shows the distribution of all nanoparticle agglomerates for aluminum nanoparticles and all the different chemical entities (polyoxo-aluminum complex, aluminum-(III)-serine, leucine aluminate and phenylalanine aluminate) separated for each chemical species. All chemical species are clearly separated from each other and located in different areas of the image as specific single agglomerates, which do not co-locate with each other. Figure S12 shows the magnified area, where predominantly Al_2O_3 NMs (shown in purple) agglomerates are located. In these areas of the DMEM with Al_2O_3 NMs single agglomerates, which do not co-localize, made of different chemical entities can be found. Figure S13 shows a magnified area, where larger agglomerates can be found, which largely consist of polyoxo-aluminum complexes and aluminum-(III)-serine. Figure S14 shows a magnification of one of the agglomerate areas. Here regions can be spotted, where polyoxo-aluminum complexes (depicted in blue) and aluminum-(III)-serine (depicted in green) co-localize (see red circles) and areas, where phenylalanine aluminate (depicted in orange) and aluminum-(III)-serine (depicted in green) co-localize (orange circles) as well as areas, where Al_2O_3 NMs (depicted in purple) and aluminum-(III)-serine (depicted in green) co-localize in the same location. These areas may be agglomerates, where a beginning mineralization combines different chemical entities in larger agglomerates.

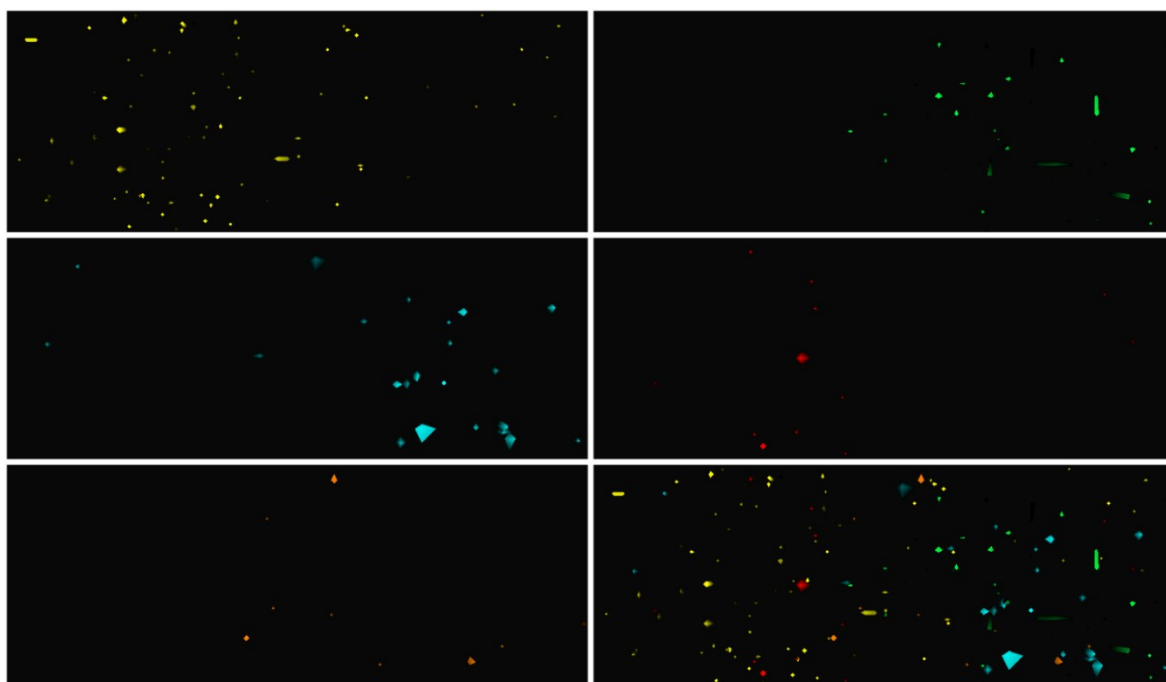


Figure S11: ToF-SIMS reconstructed ion images ($90\ \mu\text{m} \times 30\ \mu\text{m}$) of Al NMs agglomerates of different chemical entities from DMEM; yellow: Al NMs (a), green: aluminum-(III)-serine (b); orange: phenylalanine aluminate (e); red: leucine aluminate (d); blue: polyoxo-aluminum complex (c). (f) shows an overlay of all ions. In the overlay picture, all chemical entities are separated from each other and do not co-localize.

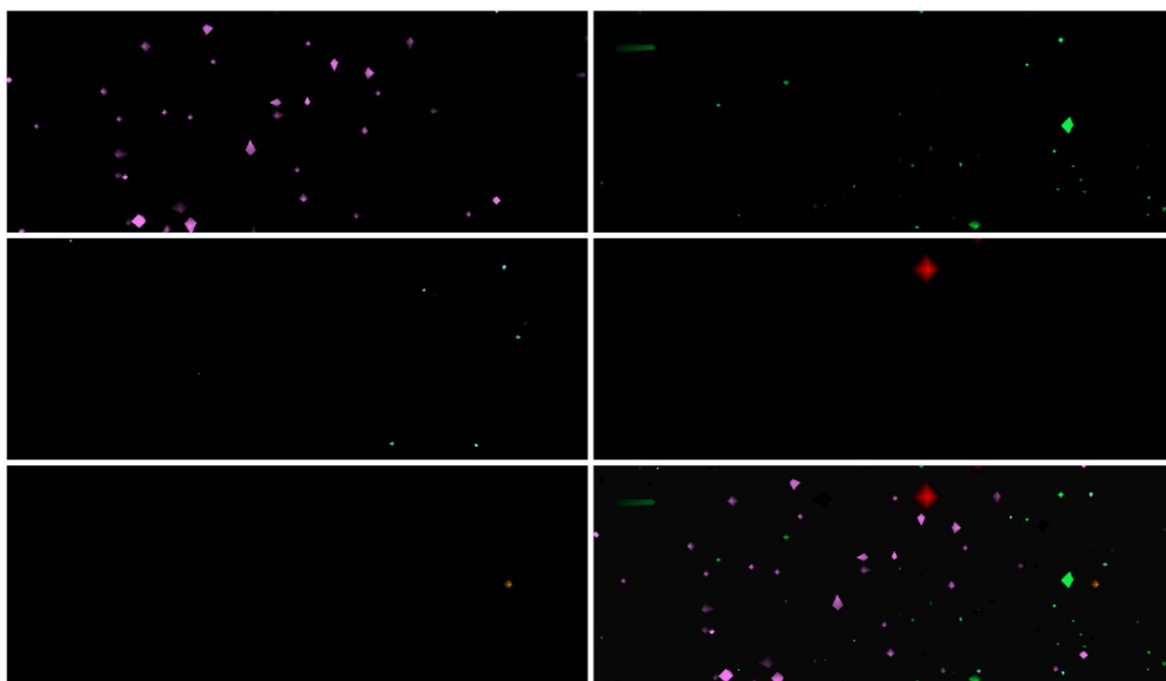


Figure S12: ToF-SIMS reconstructed ion images ($90\ \mu\text{m} \times 30\ \mu\text{m}$) of Al_2O_3 NMs agglomerates of different chemical entities from DMEM; purple: Al_2O_3 NMs (a), green: aluminum-(III)-serine (b); orange: phenylalanine aluminate (e); red: leucine aluminate (d); blue: polyoxo-aluminum complex (c). (f) shows an overlay of all ions. In the overlay picture, all chemical entities are separated from each other and do not co-localize.

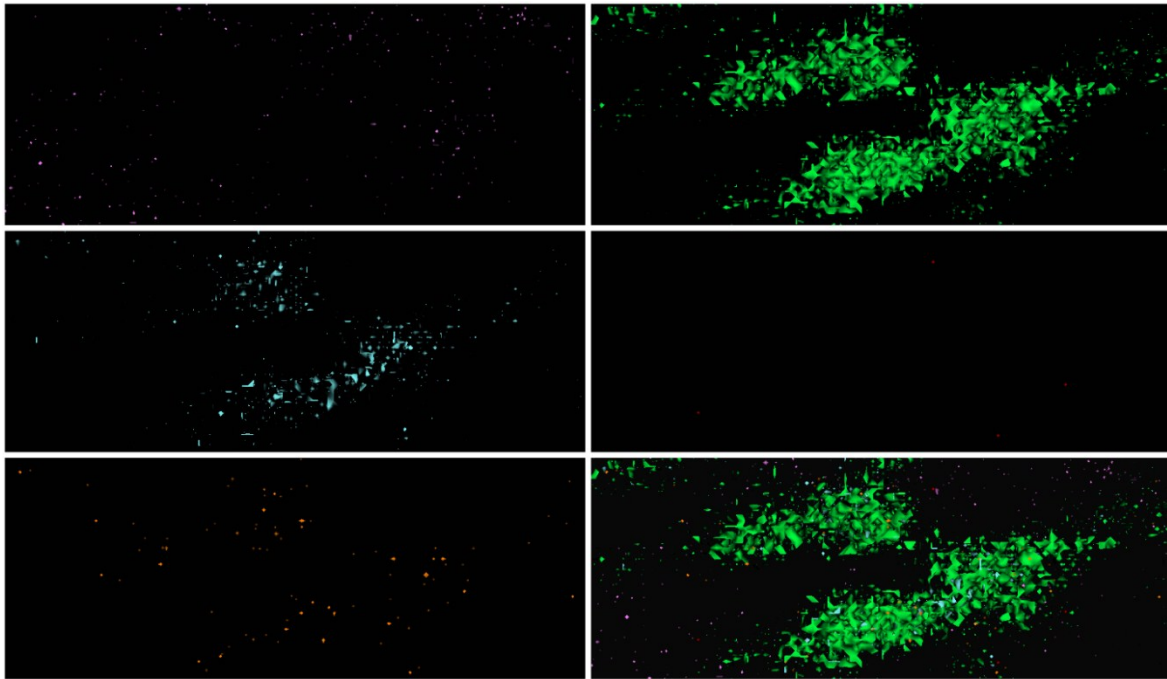


Figure S13: ToF-SIMS reconstructed ion images ($90\ \mu\text{m} \times 30\ \mu\text{m}$) of Al_2O_3 NMs agglomerates of different chemical entities from DMEM; purple: Al_2O_3 NMs (a), green: aluminum-(III)-serine (b); orange: phenylalanine aluminate (e); red: leucine aluminate (d); blue: polyoxo-aluminum complex (c). (f) shows an overlay of all ions. In the overlay picture, specific areas are visible, where predominantly polyoxo-aluminum complex and aluminum-(III)-serine co-localize in larger agglomerate areas.

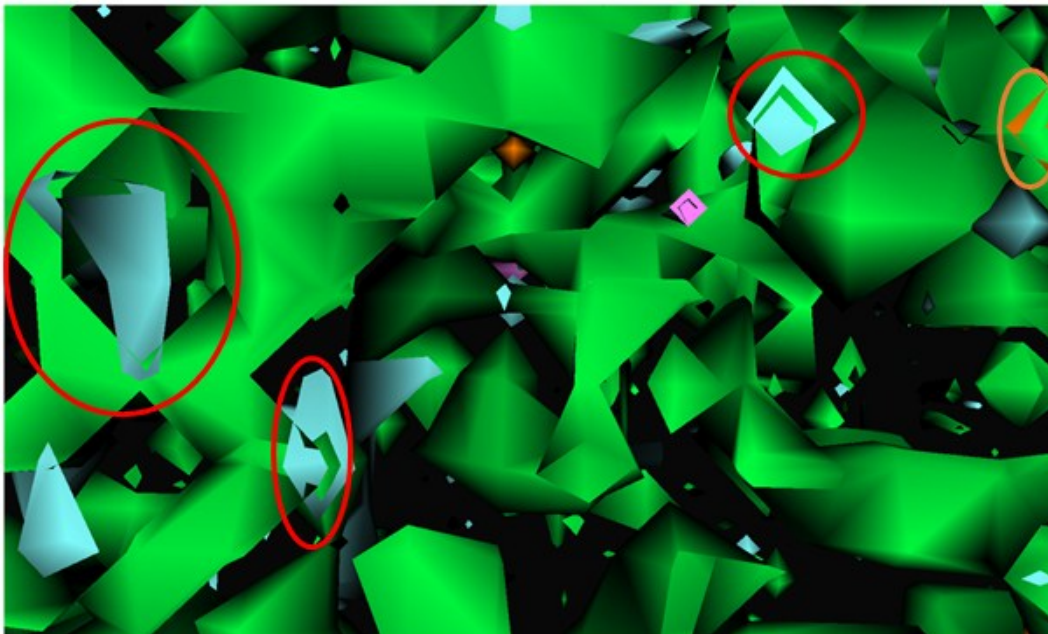


Figure S14: ToF-SIMS reconstructed ion images ($20\ \mu\text{m} \times 10\ \mu\text{m}$) of Al_2O_3 NMs agglomerates of different chemical entities from DMEM; purple: Al_2O_3 NMs, green: aluminum-(III)-serine; orange: phenylalanine aluminate; red: leucine aluminate; blue: polyoxo-aluminum complex. The picture shows an overlay of all ions. Here specific areas are visible, where polyoxo-aluminum complex (blue) and aluminum-(III)-serine (green) co-localize (see red circles) and areas, where phenylalanine aluminate (orange) and aluminum-(III)-serine (green) co-localize (orange circles) as well as areas, where Al_2O_3 NMs (purple) and aluminum-(III)-serine (green) co-localize in the same location.

Figure S15 – 18: ToF-SIMS measurements of TiO₂ NMs in DMEM

ToF-SIMS was used to visualize TiO₂ NM103 and TiO₂ NM104 as well as nanoparticle agglomerates in DMEM to assess the chemical composition of the nanoparticle agglomerates. The analyses revealed nanoparticle-specific agglomerates, consisting of TiOH⁺ amino acid complexes TiO₂ amino acid complexes were identified previously as one possible absorption mechanism and it was shown that there was selective absorption of serine on TiO₂ surfaces in benthic microbial fuel cells [4]. Also, adsorption of phenylalanine could already be observed on TiO₂ nanoparticles [5].

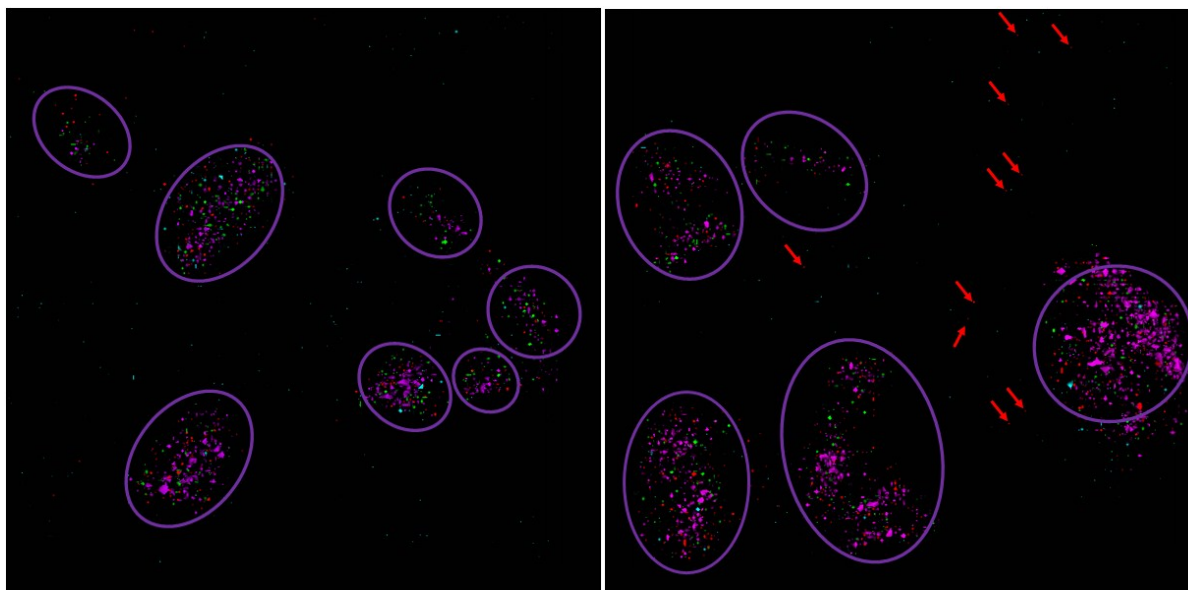


Figure S15: Left: ToF-SIMS reconstructed ion overlay image (500 μm x 500 μm) of TiO₂ NM 103 (left) and NM104 (right) agglomerates of different chemical entities from a DMEM solution; green: TiO₂ NM, blue: TiOH⁺-serine; purple: TiOH⁺-leucine; red: TiOH⁺-phenylalanine complex. Purple circles show areas where agglomerates accumulate. Red arrows show single TiOH⁺-phenylalanine aggregates outside of purple circle areas.

Figure S15 shows the ToF-SIMS image for TiO₂ NM103 (left) and TiO₂ NM104 (right). Larger agglomerate areas (purple circles in Figure S15, left and right), where TiOH⁺-leucine complexes are present in higher amounts, can be distinguished from areas with predominantly smaller NM agglomerates, made predominantly of TiOH⁺-serine in Figure S15 (left) showing TiO₂ NM103 while in Figure S15 (right), in addition to TiOH⁺-serine, TiOH⁺-phenylalanine aggregates can also be found (see red arrows in Figure S15 (right) and Figure S18). For further information about the distribution of all NM agglomerates for TiO₂ NM103 and TiO₂ NM104 and all the different chemical entities (TiOH⁺-serine, TiOH⁺-leucine, TiOH⁺-phenylalanine) separated for each chemical species, see Figures S14 and S15. All chemical species are clearly separated from each other and located in different areas of the image as specific single agglomerates, which do not co-locate with each other.

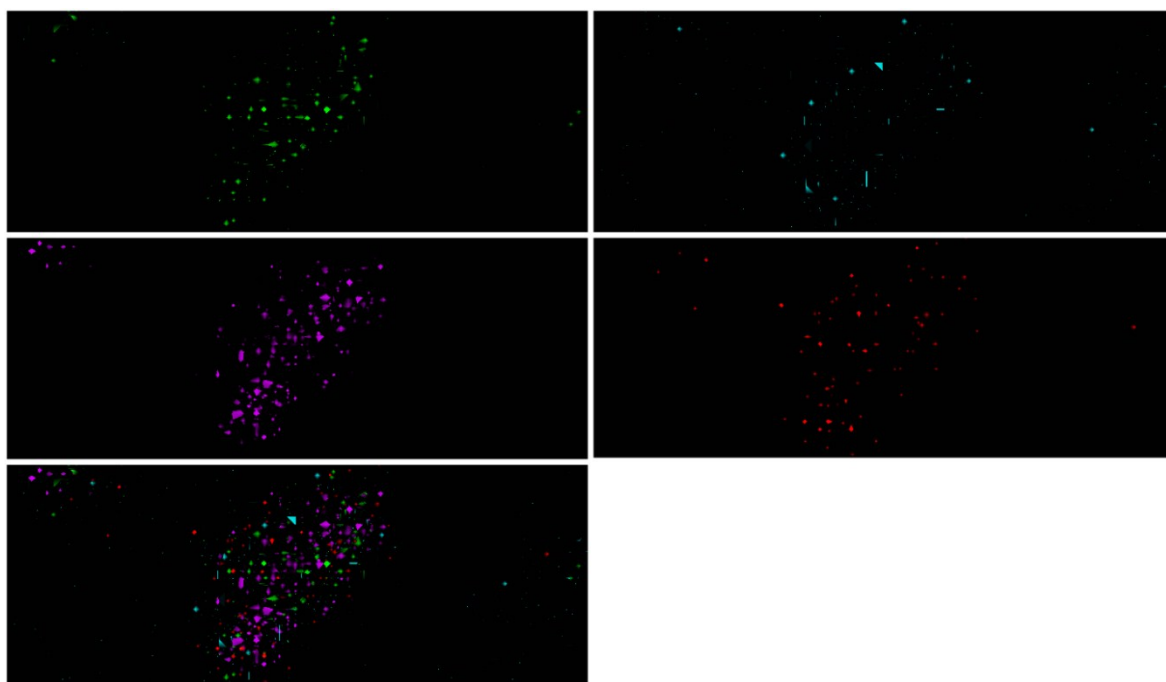


Figure S16: ToF-SIMS reconstructed ion images (90 μm x 30 μm) of TiO_2 NM-103 NMs agglomerates of different chemical entities from DMEM; green: TiO_2 NM (NM-103) (a), blue: TiOH^+ -serine (b); purple: TiOH^+ -leucine (c); red: TiOH^+ -phenylalanine (d); (e) shows an overlay of all ions. In the overlay picture, all chemical entities are separated from each other and do not co-localize.

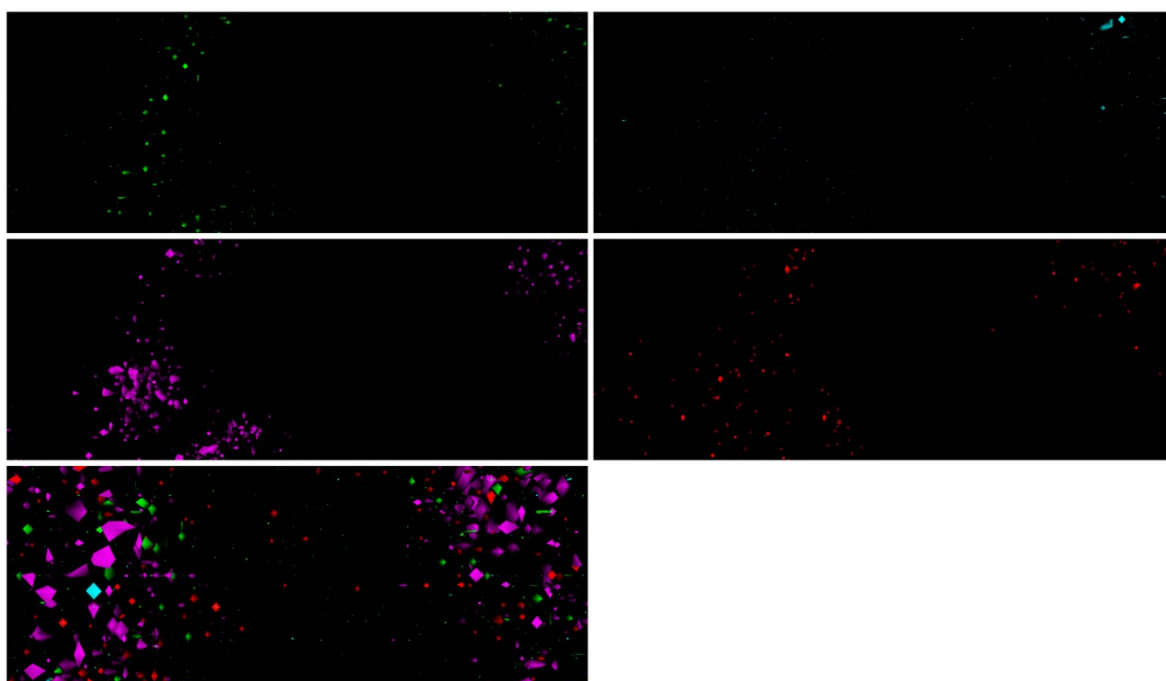


Figure S17: ToF-SIMS reconstructed ion images (90 μm x 30 μm) of TiO_2 NM-104 NMs agglomerates of different chemical entities from DMEM; green: TiO_2 NM (NM-104) (a), blue: TiOH^+ -serine (b); purple: TiOH^+ -leucine (c); red: TiOH^+ -phenylalanine (d); (e) shows an overlay of all ions. In the overlay picture, all chemical entities are separated from each other and do not co-localize.

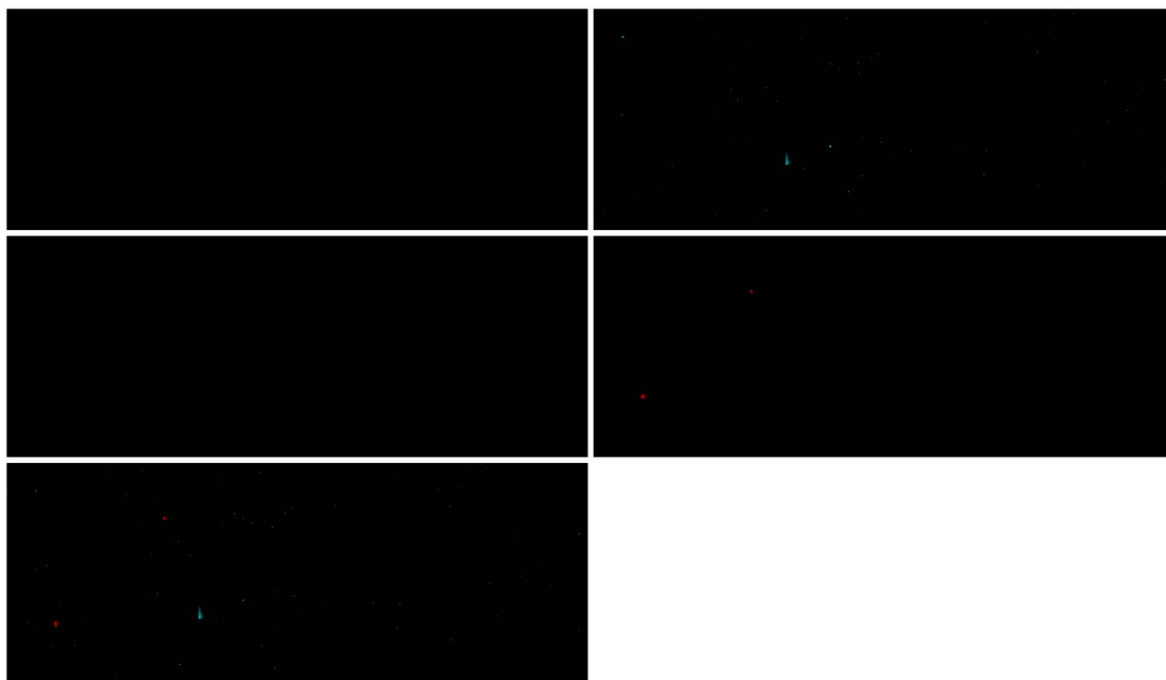


Figure S18: ToF-SIMS reconstructed ion images (90 μm x 30 μm) of TiO_2 NM-104 NMs agglomerates of different chemical entities from DMEM from an area where no agglomerate concentrations were observed; green: TiO_2 NM (NM-104) (a), blue: TiOH^+ -serine (b); purple: TiOH^+ -leucine (c); red: TiOH^+ -phenylalanine (d); (e) shows an overlay of all ions. In the overlay picture, all chemical entities are separated from each other and do not co-localize.

- [1] L.S. Sigg, W., Aquatische Chemie, Verlag der Fachvereine, Zürich, 1989.
- [2] T. Mazza, E. Barborini, P. Piseri, P. Milani, D. Cattaneo, A. Li Bassi, C.E. Bottani, C. Ducati, Raman spectroscopy characterization of TiO_2 rutile nanocrystals, *Phys Rev B* 75(4) (2007).
- [3] Z. Movasaghi, S. Rehman, I.U. Rehman, Raman spectroscopy of biological tissues, *Appl Spectrosc Rev* 42(5) (2007) 493-541.
- [4] Y.L. Zhao, C.H. Wang, Y. Zhai, R.Q. Zhang, M.A. Van Hove, Selective adsorption of L-serine functional groups on the anatase $\text{TiO}_2(101)$ surface in benthic microbial fuel cells, *Phys Chem Chem Phys* 16(38) (2014) 20806-20817.
- [5] A.G. Thomas, W.R. Flavell, C.P. Chatwin, A.R. Kumarasinghe, S.M. Rayner, P.F. Kirkham, D. Tsoutsou, T.K. Johal, S. Patel, Adsorption of phenylalanine on single crystal rutile $\text{TiO}_2(110)$ surface, *Surf Sci* 601(18) (2007) 3828-3832.